NASA Technical Memorandum 107615

MULTIFUNCTION TESTS OF A FREQUENCY DOMAIN BASED FLUTTER SUPPRESSION SYSTEM

David M. Christhilf and
William M. Adams, Jr.

MAY 1992

NASA
National Aeronautics and
Space Administration

Langley Research Center
Hampton, VA 23665

MULTIFUNCTION TESTS OF A FREQUENCY DOMAIN BASED FLUTTER SUPPRESSION SYSTEM

David M. Christhilf *
Lockheed Engineering & Sciences Company, Hampton, Virginia 23666

William M. Adams, Jr.†
NASA Langley Research Center, Hampton, Virginia 23665

Abstract

This paper describes the process of analysis, design, digital implementation and subsonic testing of an active controls flutter suppression system for a full span, free-to-roll wind-tunnel model of an advanced fighter concept. The design technique employed a frequency domain representation of the plant and used optimization techniques to generate a robust multi-input/multi-output controller. During testing in a fixed-in-roll configuration, simultaneous suppression of both symmetric and antisymmetric flutter was successfully demonstrated. For a free-to-roll configuration, symmetric flutter was suppressed to the limit of the tunnel test envelope. During aggressive rolling maneuvers above the open-loop flutter boundary, simultaneous flutter suppression and maneuver load control were demonstrated. Finally, the flutter suppression controller was reoptimized overnight during the test using combined experimental and analytical frequency domain data, resulting in improved stability robustness.

Introduction

An advanced fighter aircraft design which exploits, rather than avoids, wing flexibility to provide improved aerodynamic performance is likely to require an active flutter suppression system (FSS) to remove dynamic structural instabilities (particularly if FSS is employed in the design process to minimize weight). If the FSS is required for stabilization within the operational envelope, it is essential that proper FSS functioning be maintained during aggressive maneuvers. This paper describes the design and wind-tunnel test of an active FSS for a configuration that exploits wing flexibility. Reliability aspects are not addressed.

The test vehicle used in the study was the Active Flexible Wing (AFW) wind-tunnel model built by Rockwell.[1] Testing was conducted in the NASA Langley Research Center Transonic Dynamics Tunnel (TDT). The model (see fig. 1) was sting mounted and could be rolled about the sting axis (free-to-roll configuration) between plus and minus 145 degrees. Roll motion could be prevented through the use of a mechanical pin prior to testing, or stopped during a maneuver through the use of a hydraulically actuated roll brake (fixed-in-roll configuration).

Active controls flutter suppression of the AFW wind-tunnel model was tested during TDT entries, in 1989 and 1991,[2] using a dedicated programmable digital controller.[3] For the 1989 entry, only the fixed-in-roll configuration was tested for plant identification and for flutter suppression.[4,5] Results in the present paper pertain to the 1991 entry, the primary objective of which was to demonstrate simultaneous application of digitally implemented multi-input/multi-output (MIMO) flutter suppression and maneuver load controllers while performing aggressive rolling maneuvers above the open-loop flutter boundary.

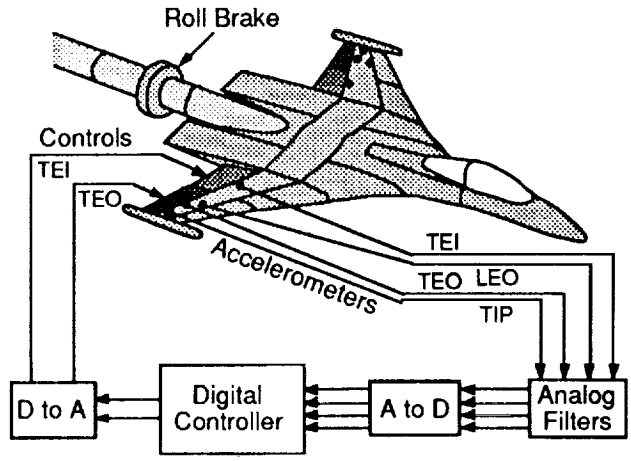

Fig. 1 Sketch of AFW wind-tunnel model.

Flutter suppression testing was conducted subsonically in air, operating at atmospheric static pressure. For the fixed-in-roll configuration, both symmetric and antisymmetric flutter were predicted to occur within the TDT operating capability. For the free-to-roll configuration, only symmetric flutter (unaffected by roll freedom status) was predicted to occur within the TDT operating capability. Thus, one control law was developed to suppress symmetric flutter and another was developed to suppress fixed-in-roll antisymmetric flutter. Both control laws were active, operating in parallel, for fixed-in-roll flutter suppression testing. Only the symmetric law was active for the free-to-roll tests.

Modeling

Linear mathematical models were generated for design and preliminary evaluation of candidate controllers. The Interaction of Structures, Aerodynamics and Controls (ISAC) system of programs [6,7,8] played a key role in providing linear models (see fig. 2). ISAC received inputs that included in vacuo modal data, planform geometry, aerodynamic paneling specifications, turbulence power spectral density characterizations, sensor locations, and actuator transfer function descriptions. It then provided linear aeroelastic equations of motion at specified conditions for use in analysis and design. A frequency domain form of the equations of motion made direct use of tabular unsteady aerodynamic forces computed using a doublet lattice code contained within ISAC. A finite dimensional state space form employed rational function approximations of the unsteady aerodynamic data.[8]

* Engineer, Langley Program Office, 144 Research Drive. Member AIAA.
† Senior Research Engineer, 6 N. Dryden Street, MS 489. Associate Fellow AIAA.

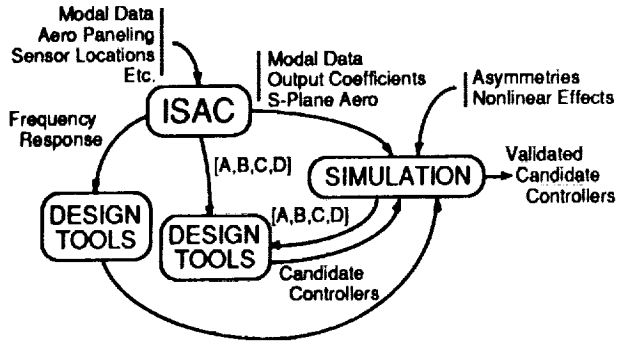

Fig. 2 Modeling via ISAC.

Closed-loop operation of the candidate controllers was validated prior to wind-tunnel testing with simulation analyses. ISAC provided intermediate, linear, mathematically generated data necessary for the creation of the simulations (see fig. 2). The simulations then incorporated separate left and right models for the actuators, actuator deflection and rate limits, and quantization effects for the analog/digital conversion process. [9,10,11] State space models could be extracted from the simulation for control law design purposes by perturbing the simulation model. The simulation allowed both symmetries to be run simultaneously in the presence of independently generated symmetric and antisymmetric turbulence.

The frequency domain form of the equations of motion was employed in development of the controller design discussed herein. This form of the equations allowed numerical computation of a frequency response for any output/input pair and direct replacement with experimental data when they became available. The frequency domain form of the equations of motion was presented in reference 4.

Modal data from a structural model developed prior to the 1989 TDT entry were employed in generating the equations of motion used for analysis and design. This selection was made in preference to a post-1989 model that was also available because the character of the resulting analytical frequency response predictions was in closer agreement with experiment, and both models exhibited comparable levels of inaccuracy in predicting the flutter frequencies.

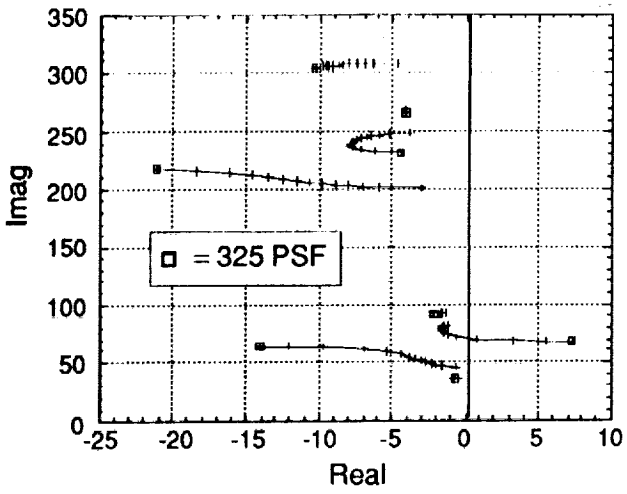

Fig. 3 Root locus.
(symmetric, open-loop, dynamic pressure variation)

Flutter and Input/Output Characteristics

Analyses were made, using the linear mathematical models, of the predicted stability and response characteristics of the AFW wind-tunnel model in order to determine the flutter characteristics and to assess candidate controls and sensors to use in the control laws. The trailing edge outboard (TEO) and trailing edge inboard (TEI) pairs of control surfaces (see fig. 1) were effective for flutter suppression. Each pair of wing accelerometers was characterized in terms of its location, the leading edge outboard (LEO), trailing edge inboard (TEI), trailing edge outboard (TEO), and wingtip (TIP) pairs. Key analysis results are presented below.

Figure 3 presents loci of symmetric poles generated by varying dynamic pressure, expressed in pounds per square foot (psf), from 0 psf to 325 psf in 25 psf increments. The analysis was performed using a linear state space representation that contained single-lag rational function approximations of the unsteady aerodynamic forces. The loci of poles depicts a primary flutter mechanism that is an example of classical airplane flutter, with approximate coalescence (near 70 radians

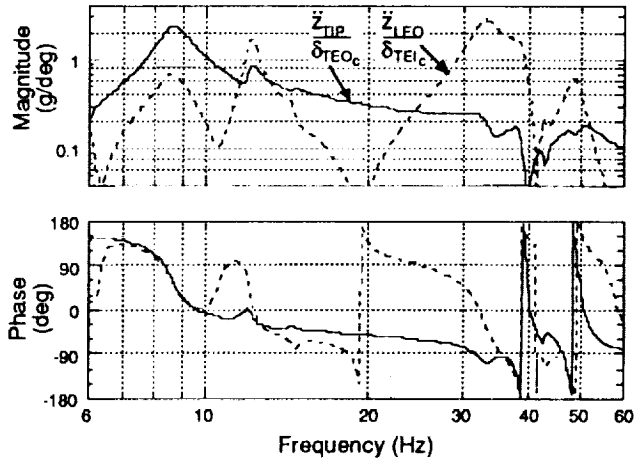

Fig. 4 Frequency responses.
(symmetric, open-loop, 175 psf)

per second) of the damped frequencies of two roots corresponding to modes that, in vacuo, were predominantly first wing bending and first wing torsion. The predicted flutter dynamic pressure was 248 psf. A second pole, near 230 radians per second, was approaching instability at 325 psf, indicating the presence of a secondary flutter mechanism. The significant, although smaller than desirable, frequency separation between the primary and secondary flutter mechanisms facilitated the task of primary flutter suppression without secondary flutter degradation.

Figure 4 presents information typical of that used to select control surfaces and sensors to employ in the controller. Bode plots are presented for two of the symmetric components ($\ddot{z}_{TIP}/\delta_{TEO_c}$ and $\ddot{z}_{LEO}/\delta_{TEI_c}$) of the AFW element shown in figure 5, at a dynamic pressure of 175 psf. Inspection of this figure indicated that $\ddot{z}_{LEO}/\delta_{TEI_c}$ had the undesirable property of responding to modes in the higher, secondary flutter frequency range. The undesirable high frequency response was present for all sensors other than those at the wingtip. The $\ddot{z}_{TIP}/\delta_{TEO_c}$ transfer function exhibited desirable high frequency rolloff. However, the primary flutter mode was more in evidence for $\ddot{z}_{LEO}/\delta_{TEI_c}$ than for $\ddot{z}_{TIP}/\delta_{TEO_c}$. The

relative prominence of the flutter mode among the various transfer functions was strongly influenced by the variation in location of a critical, lowly damped zero relative to the pole that became unstable (see reference 12 for a discussion of the impact of the critical zero upon controller design). The analysis indicated that all of the wing accelerometers, with appropriate high frequency filtering, were viable candidates for feedback.

For the fixed-in-roll configuration, the loci of antisymmetric poles (not shown) exhibited behavior similar to that of figure 3 with predicted flutter at about the same frequency and with onset (≈252 psf) that was higher in dynamic pressure by only about 1.6 percent. Likewise, the frequency separation between the primary flutter mechanism and a cluster of higher frequency modes was similar to that of the symmetric case.

Pretest Design Activity

The design philosophy adopted was to seek an unscheduled, MIMO flutter suppression controller. The design was accomplished in the continuous domain although the controller was implemented digitally using a Tustin transformation. A number of design considerations were addressed.

Design Considerations

Three dynamic elements that will recur in the discussion of controller dynamics (a general second-order element, a first-order highpass element, and a first-order lowpass element) are defined here as

$$e = e(\zeta_n, \zeta_d, \omega_n, \omega_d)$$

$$= (s^2 + 2\zeta_n \omega_n s + \omega_n^2) / (s^2 + 2\zeta_d \omega_d s + \omega_d^2), \quad (1)$$

$$HP = HP(a) = s / (s + a), \quad (2)$$

$$LP = LP(c) = c / (s + c), \quad (3)$$

where s is the Laplace variable, ζ_n and ζ_d are numerator and denominator damping ratios, respectively, ω_n and ω_d are numerator and denominator natural frequencies, respectively, a is the highpass filter pole, and c is the lowpass filter pole.

The frequency separation between the roll degree-of-freedom and the flutter mechanism was sufficiently large to conclude that FSS and load-limiting rolling maneuver control laws could safely be designed separately and then operated simultaneously provided filtering was included to prevent interference. Accordingly, highpass dynamic elements (HP, eq. (2)) were included in the FSS controller to ensure low frequency separation by attenuating any low frequency disturbance to or from the load-limiting active control law. A lowpass filter (LP, eq. (3)), with break frequency well below 10 Hz, in the maneuver load control (MLC) system would complete the frequency separation objectives.

Figure 5, which refers to either of the symmetries of motion (symmetries were decoupled in the linear models), indicates that all four accelerometers on each wing were used in the feedback control law to drive both trailing edge control surfaces. Multiple sensors and control surfaces were used both to satisfy program MIMO objectives and to exploit the favorable characteristics of the various sensors and controls that were seen in the analysis discussed previously. Attenuation of undesirable high frequency sensor signal components in accelerometers other than $\ddot{z}_{TIP}$ was accomplished using available analog notch filters, $N_P(s) = e(0.08, 0.32, 2\pi (32), 2\pi (32))$, see eq. (1).

The sample rate for digitally implemented controllers was prescribed to be 200 Hz. To reduce aliasing, a first-order analog filter with break frequency of 25 Hz (157 rad/sec) was incorporated on each channel to be sampled. These

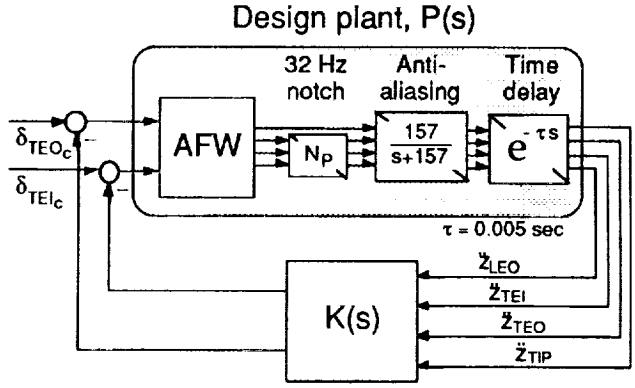

Fig. 5 Design plant definition.

antialiasing filters also provided some attenuation between 25 and 100 Hz and, thereby, reduced signal strength in the range of higher frequency structural modes. Phase lag at 10 Hz (near the flutter frequency) due to this filter was about 22 degrees.

The plant used in design of the continuous controller (see fig. 5) contained analog notch and antialiasing filters and an additional time delay element that was included to compensate for effects of digital implementation. Since, in actual digital implementation, some time would be required to generate control command outputs after receipt of sensor inputs, the control laws were implemented in the digital controller such that control commands generated based upon sensor inputs received at one sampling instant were held until the next sampling instant. Therefore, a net delay of 1-time step associated with holding the controller output was included in the "design plant" model. This amounted to a phase lag of 18 degrees at 10 Hz.

Use of an unscheduled controller required closed-loop stability over the full test range of dynamic pressures (100 psf-to-325 psf) based upon the analytical simulation model. Gain margins of ± 4 dB and phase margins of ±30 degrees, or their multivariable equivalents, were also required over this range. In addition, stability in the presence of ±10 percent variations in the frequencies of the coalescing modes was required at a 300 psf evaluation point. A design point of 325 psf was chosen.

Actuator rate saturation can effectively induce lag and reduce the amplitude of control surface deflections. At 325 psf, the open-loop time-to-double amplitude was predicted to be about 1/10 of a second. For this level of instability, actuator rate saturation of a pair of actuators for even a brief period of time in response to wind-tunnel turbulence could cause unacceptably large growth of the flutter mode. This reinforced the need for restriction on actuator rate requirements. The TEO surfaces were conservatively assumed to have a no-aerodynamic load rate limit of 150 degrees per second. It was assumed that no rate saturation for a 3-standard deviation turbulence velocity magnitude was adequate for assuring that actuator rate saturation was sufficiently unlikely. This constrained the RMS rate for a 1-standard deviation turbulence velocity to be less than 50 degrees per second. Definition of the assumed turbulence characteristics is presented in reference 11.

Design Approach

In this section the approach taken to determine the controller, K(s), is outlined. The approach was the same for each symmetry and separate designs were obtained. The first step was to explicitly specify the controller structure, including all dynamic elements, thereby displaying selectable design

variables. Optimization techniques were employed to select values for the design variables. The optimization process took place in two distinct stages. For each stage, a conjugate gradient algorithm [13,14,15] was used to minimize a cost function representing dissatisfaction with respect to a set of design criteria. For the first stage a dominant control surface/sensor pair was selected. The trailing edge outboard control surfaces and the accelerometer pair nearest the wing tips were selected because the combination exhibited desirable high frequency rolloff characteristics and adequate response in the flutter frequency range at the 325 psf design point. Parameters determining the controller dynamics were then optimized for this single-input/single-output (SISO) compensator to increase tolerance to multiplicative and additive plant errors and to increase tolerance to errors in the predicted flutter frequency. The second stage, employing fixed dynamics from the first stage, determined the coefficients used for blending the four pairs of sensors into one composite sensor and for distributing the filtered feedback signal to the two pairs of controls. The choice of blending and distribution coefficients was made so as to achieve MIMO robustness to additive plant errors and to errors at plant input and output.

SISO Optimization

The form of the SISO compensator for the first stage optimization is shown in figure 6. There was an overall gain, (k_1), a highpass element ($HP_1(a_1)$) that has already been discussed, a broad notch ($N_F = e(\zeta_{nN}, \zeta_{dN}, \omega_N, \omega_N)$) that reduced the observability of the coalescing pole that became more damped, a bandpass (amplification) element ($A_F = e(\zeta_{nA}, \zeta_{dA}, \omega_A, \omega_A)$) that partially removed the negative impact of a critical zero in the flutter frequency range (refs. 4 and 12), a higher frequency notch to avoid adversely affecting higher frequency modes, and a lowpass element for rolloff. The higher frequency notch and lowpass elements were unity at this stage and will be discussed below, where first used.

SISO Design and Cost Function Variables. The eight design variables used in the SISO optimization were

$(k_1, a_1, \zeta_{nN}, \zeta_{dN}, \omega_N, \zeta_{nA}, \zeta_{dA}, \omega_A)$.

The highpass frequency was constrained to be between 10 and 25 rad/sec, and all damping ratios were constrained to be between 0.1 and 1. These design variable constraints were enforced through a trigonometric mapping technique.[16]

The dependent variables used to form the cost function were:

$$\hat{\sigma}_o \equiv \min_{\omega} \{ \text{abs}[\, 1 + f_o(i\omega) \,] \}$$

$$\hat{\sigma}_p \equiv \min_{\omega} \{ \text{abs}[\, 1 + f_o(i\omega) \,] / \text{abs}[\, k(i\omega) \,] \}, \text{ g/deg}$$

$$L \equiv \begin{cases} \text{True if closed-loop stable} \\ \text{False if closed-loop unstable} \end{cases}$$

where ω varied from 10-to-400 rad/sec (1.6-to-64 Hz). The symbols $p(i\omega)$, $k(i\omega)$, and $f_o(i\omega) = p(i\omega)\,k(i\omega) = k(i\omega)\,p(i\omega)$ represented frequency responses for the SISO plant, controller and loop-transfer functions, respectively (see fig. 6). The variables $\sigma_o(\omega)$ and $\sigma_p(\omega)$ were singular values which represented tolerance to unstructured multiplicative error and to unstructured additive plant error, respectively. The ($\hat{}$) represented the minimum over the range of frequencies considered. The logical variable, L, indicated whether the closed-loop system was stable. Closed-loop stability was computed by knowing the stability of the open-loop plant and requiring the appropriate number of counterclockwise encirclements of the critical point (-1) for a polar (complex plane) plot of $f_o(i\omega)$.

Terms were included in the cost function to desensitize the controller to errors in the predicted frequencies of the poles that coalesced to produce flutter. Design criteria were specified not only for the nominal plant, but also for eight variational plants obtained by perturbing the frequency of at least one of the two coalescing poles by ±10 percent. The variational plants were not generated. Instead, an alternate, approximately equivalent approach was adopted: namely perturbing the frequencies of related compensator variables. The frequency of the amplification element was perturbed to mimic a corresponding frequency shift in the opposite direction for the plant pole that was unstable. Likewise, the frequencies for the notch and the highpass elements were perturbed in unison to mimic a shift in the frequency of the stable coalescing plant pole. Each iteration of the optimization required evaluation of the cost function components for the nominal compensator and its eight variations.

During early stages of the study, RMS control surface rates had been computed for inclusion in the cost function, but were removed from the optimization after observing that they rarely exceeded the 50 deg/sec design requirement.

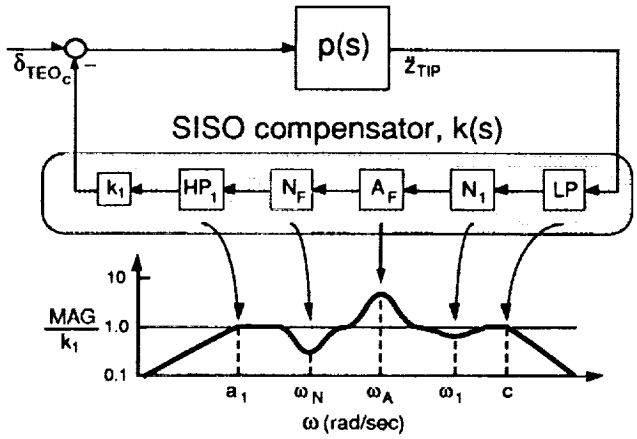

Fig. 6 SISO controller dynamics.

SISO Cost Function and Component Scaling. The design variables were scaled to improve the mathematical conditioning of the optimization, but proper scaling of the dependent variables used in forming the cost function was more important. The scaling of these cost function components had a direct impact on the solution achieved. The cost function had the form:

$$J_{SISO} = V_{o_1}{}^4 + V_{p_1}{}^4 + \sum_{m=2}^{9} \{ V_{o_m}{}^2 + V_{p_m}{}^2 \} \qquad (4)$$

where m was an index indicating either nominal (m = 1) or perturbed (m = 2-to-9) compensator dynamics. V_o and V_p were scaled violations of constraints, defined as follows:

If L_m was true (stability)

$V_{o_m} = S_o \max(0, T_{o_m} - \hat{\sigma}_{o_m})$,

$V_{p_m} = S_p \max(0, T_{p_m} - \hat{\sigma}_{p_m})$,

otherwise

$V_{o_m} = U_o (T_{o_m} + \hat{\sigma}_{o_m})$,

$V_{pm} = U_p\ (T_{pm} + \hat{\sigma}_{pm})$,
where

$S_o = 10$, $S_p = 10$ deg/g were scale factors if stable,

$U_o = 14$, $U_p = 14$ deg/g were scale factors if unstable,

$T_{o_1} = 0.9$, $T_{p_1} = 0.9$ g/deg were target min. sing. values,

$T_{o_m} = 0.6$, $T_{p_m} = 0.6$ g/deg were target min. sing. values,

for $m > 1$.

Some comparisons can be made between nominal (m = 1) and variational (m = 2-to-9) terms in the cost function (see eq. (4)). The nominal terms were emphasized by selection of larger target minimum singular value magnitudes (0.9 vs 0.6). The selection of unachieved 0.9 magnitudes caused the nominal scaled violations V_{o_1} and V_{p_1} to exceed 1 throughout the optimization. Consequently, raising these nominal scaled violations to the fourth power in the cost function, as compared with only squaring the variational scaled violations, further accentuated the nominal case.

Equal target minimum singular value magnitudes and equal scale factor magnitudes were chosen for plant additive error and loop transfer function multiplicative error despite the dimensional incompatibility. This choice was made because, for prototype stabilizing SISO compensators, the smallest values for $\sigma_p(\omega)$, in g/deg, and for $\sigma_o(\omega)$ were of comparable size. Different target magnitudes and different scale factor magnitudes would generally be required for variables having disparate magnitude ranges.

Table 1 Tolerance to flutter frequency and gain variations (symmetric, 300 psf, S = stable, U = unstable, SISO)

Δk_1	− 4 dB			0 dB			+ 4 dB		
ω_1 \ ω_2	×0.9	×1.0	×1.1	×0.9	×1.0	×1.1	×0.9	×1.0	×1.1
×0.9	U	S	S	S	S	S	S	S	S
×1.0	S	S	S	S	S	S	S	S	S
×1.1	S	S	S	S	S	S	S	S	S

Cost function component definitions changed at the stability boundary such that singular values were driven smaller rather than larger for the closed-loop unstable condition. Thus, the requirement for an initially stabilizing selection of parameters for the nominal controller and all of its variations was relaxed. Furthermore, scale factor changes produced a discrete jump in the cost at the stability boundary. A scale factor discontinuity was acceptable in this case because the stability boundary was not a satisfactory solution. As a result of the discrete jump and the composition of the performance function, once a stabilizing controller was achieved, destabilizing controllers were removed from consideration.

SISO Performance Predictions. Table 1 summarizes the results of the SISO optimization for the symmetric control law in terms of closed-loop insensitivity to frequency variations in the open-loop plant. The closed-loop system was stable at 300 psf (the required evaluation point) for all variational combinations of the frequencies, and had 4 dB or more gain margin for all combinations except one, as indicated.

Figure 7 presents Nyquist plot evaluations of the antisymmetric SISO nominal and variational controllers at 300 psf (open-loop unstable, critical point at -1). The solid curve is for the nominal case. This figure shows that all variational controllers are stable with gain margins exceeding ± 4 dB. The figure also contains the information needed for determination of phase margins, minimum singular value and maximum loop gain for each of the nine controllers.

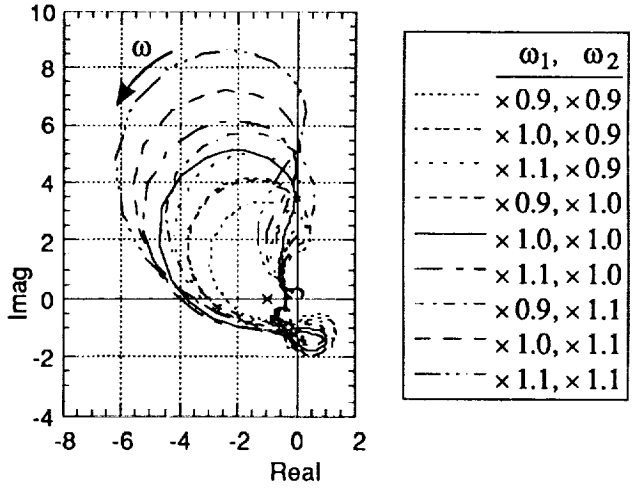

Fig. 7 Nyquist plots for SISO controllers. (fixed-in-roll, antisymmetric, 300 psf)

MIMO Optimization

The second stage of the optimization pertained to the MIMO controller. As shown in figure 8, four pairs of sensors and two pairs of control surfaces were employed. The dynamic elements N_1, N_2, and LP were unity at this stage. They will be discussed below, where first used. The dynamic elements found during the SISO optimization were retained, unchanged, in the $\delta_{TEO_c}/\ddot{z}_{TIP}$ channel. However, for the channel containing information from the other three sensor pairs, the highpass break frequency (a_2 in HP_2) was increased as compared to a_1. The selection of a_2 was made such that, at the flutter frequency, the additional lead compensated for the lag due to the 32 Hz analog notch filter (see figure 5) on each of the three pairs of inboard sensor channels. This produced phase matching at the flutter frequency for the primary and the notched sensor channels, at the expense of reduced phase margins for the notched channels.

MIMO Design and Cost Function Variables. The design parameters for the MIMO optimization were the overall gain,

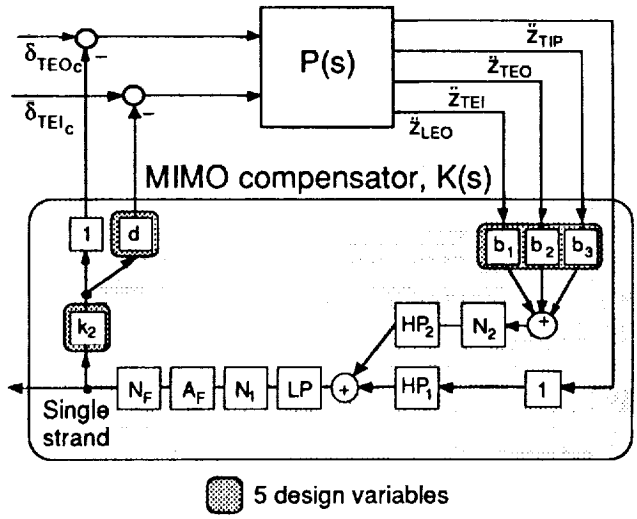

Fig. 8 MIMO controller structure.

(k_2), the blending coefficients for the inboard sensor pairs (b_1, b_2, b_3), and the distribution coefficient (d) for the inboard control surface pair. These five parameters are shaded in figure 8. No constraints were imposed on the design parameters.

The dependent variables used to form the cost function components were:

$$\hat{\underline{\sigma}}_s \equiv \min_{\omega} \left\{ \underline{\sigma} [\, I_{4\times4} + P(i\omega)\, K(i\omega) \,] \right\}$$

$$\hat{\underline{\sigma}}_c \equiv \min_{\omega} \left\{ \underline{\sigma} [\, I_{2\times2} + K(i\omega)\, P(i\omega) \,] \right\}$$

$$\hat{\underline{\sigma}}_p \equiv \min_{\omega} \left\{ 1 \;/ \bar{\sigma} \left[K(i\omega) \left[I_{4\times4} + P(i\omega)\, K(i\omega) \right]^{-1} \right] \right\}, \text{ g/deg}$$

$$B \equiv \begin{cases} 0 & \text{if closed-loop stable} \\ 100 & \text{if closed-loop unstable} \end{cases}$$

where $\sigma[\ ]$ denoted the operation of finding the singular values of the matrix within the brackets, $(\underline{\ })$ and $(\bar{\ })$ denoted minimum and maximum, respectively, and, as in the SISO case, $(\hat{\ })$ denoted the minimum over ω. The indicated minimization over ω covered the frequency range from 10-to-400 rad/sec (1.6-to-64 Hz). Symbols $P(i\omega)$ and $K(i\omega)$ represented frequency response matrices for the 2-input, 4-output plant and for the 4-input, 2-output compensator, respectively (see fig. 8). The functions $\underline{\sigma}_s(\omega)$ and $\underline{\sigma}_c(\omega)$ were minimum singular values of plant output and input return difference matrices which represented tolerance to unstructured multiplicative error at the sensors and at the controls, respectively.[17] The function $\underline{\sigma}_p(\omega)$, in g/deg, was the reciprocal of a maximum singular value and represented tolerance to unstructured additive plant error.

The variable B was a penalty to be added to the cost function if a candidate set of design variables caused closed-loop instability. Stability was checked at each iteration after evaluating the frequency response, $f_{ss}(i\omega)$, of the loop transfer function at the single strand point identified in figure 8. Closed-loop stability was computed by knowing the stability of the open-loop plant and requiring the appropriate number of counterclockwise encirclements of the origin for a polar plot of $[1+f_{ss}(i\omega)]$. (Although this was a reliable indicator of absolute stability, stability margins defined at the single strand point were potentially nonconservative[4] and, therefore, were not used).

MIMO Cost Function and Component Scaling. Values of the design variables were sought which minimized the following cost function (only fixed, nominal compensator dynamics were considered)

$$J_{MIMO} = V_s^2 + V_c^2 + V_p^2 + B,$$

where

$$V_s = S_s \max(0, T_s - \hat{\underline{\sigma}}_s)$$

$$V_c = S_c \max(0, T_c - \hat{\underline{\sigma}}_c)$$

$$V_p = S_p \max(0, T_p - \hat{\underline{\sigma}}_p)$$

where

$S_s = S_c = 10$, and $S_p = 10$ deg/g were scale factors, and

$T_s = T_c = 0.6$, and $T_p = 0.6$ g/deg were target min. sing.vals.

As in the SISO case, selection of equal scale factor magnitudes and equal target lower bound magnitudes for each of the dimensional and nondimensional variables was based upon the various minimum singular values having approximately the same magnitudes.

Since the MIMO optimization used zero starting values for the blending coefficients for the additional sensors and controls, and since the initial SISO controller was known to stabilize the closed-loop system, no provision was made to drive singular values smaller for a closed-loop unstable situation. Rather, consideration of closed-loop unstable controller coefficients was precluded by making the stability boundary approach the characteristics of a hard constraint through the use of the large discrete jump (B) in the cost function.

For each symmetry, the controller that was obtained as a result of the MIMO optimization process was predicted to suppress flutter over the anticipated test range of dynamic pressures, to satisfy all robustness criteria, and to call for RMS actuator rates that were well within the 50 deg/sec design requirements.

MIMO Simulation and Controller Adjustment. Candidate control laws designed based upon linear models at 325 psf were evaluated over the anticipated test range of dynamic pressures using the nonlinear simulations. The closed-loop system was stable at all points for both fixed and free-to-roll configurations. However, the gain (k_2) was adjusted more toward the center of its stable range. In addition, notch filters (N_1) were added at the single strand point (see fig. 8) to reduce transient, turbulence induced responses observed in the 20 Hz-to-50 Hz frequency range. The notches added (which were to be implemented digitally after the prewarping discussed below) were $N_1(s) = e(0.40,\ 0.60,\ 2\pi\ (23.9),\ 2\pi\ (23.9))$ symmetrically and $N_1(s) = e(0.20,\ 0.60,\ 2\pi\ (50.0),\ 2\pi\ (50.0))$ antisymmetrically. New experimentally determined actuator transfer function estimates were incorporated which, fortuitously, approximately compensated for the phase lag due to the added notches, removing the need for reoptimization.

Figure 9 shows time histories generated using the simulation from reference 9 for a candidate pretest control law that did not have the notches, N_1. The results represent a fixed-in-roll condition, with no turbulence input, at the design point of 325 psf. Beginning at 0.1 second, a 10 Hz

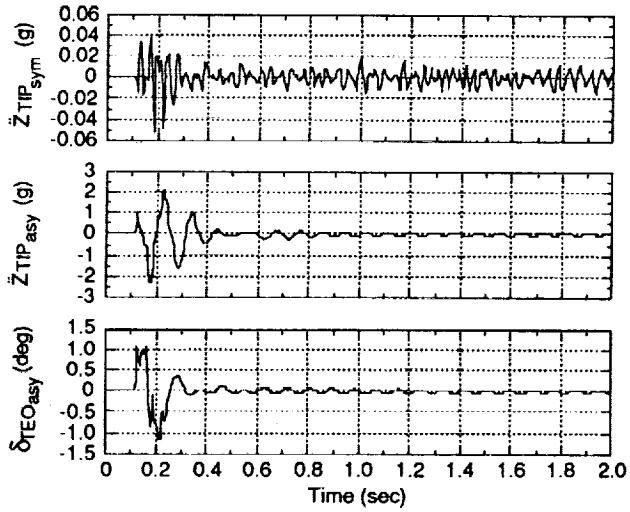

Fig. 9 Nonlinear simulation performance.
(fixed-in-roll, 325 psf, no turbulence)

Table 2 Parameter values for final controller

	Symmetric	Antisymmetric
HP_1	a_1 = 10.0 1/sec	a_1 = 10.0 1/sec
N_F	ζ_{n_N} = 0.20	ζ_{n_N} = 0.14
	ζ_{d_N} = 0.57	ζ_{d_N} = 0.33
	ω_{n_N} = 47.1 rad/sec	ω_N = 44.0 rad/sec
	ω_{d_N} = 44.6 rad/sec	
A_F	ζ_{n_A} = 0.55	ζ_{n_A} = 0.37
	ζ_{d_A} = 0.12	ζ_{d_A} = 0.12
	ω_{n_A} = 68.5 rad/sec	ω_A = 69.7 rad/sec
	ω_{d_A} = 64.7 rad/sec	
N_1 [a]	ζ_{n_1} = 0.40	ζ_{n_1} = 0.20
	ζ_{d_1} = 0.60	ζ_{d_1} = 0.60
	ω_1 = 150 rad/sec	ω_1 = 314 rad/sec
LP [a]	c = 364 1/sec	not used
HP_2	a_2 = 23.2 1/sec	a_2 = 18.2 1/sec
N_2 [a]	ζ_{n_2} = 0.16	not used
	ζ_{d_2} = 0.48	not used
	ω_2 = 251 rad/sec	not used
Gain Coefs	k_2 = 0.697 deg/g	k_2 = 0.675 deg/g
	b_1 = 0.586	b_1 = 0.331
	b_2 = 0.006	b_2 = 0.213
	b_3 = 0.265	b_3 = 0.437
	d = 0.453	d = 0.552

[a] prior to prewarping.

antisymmetric doublet command of 1 degree magnitude was input to the TEO actuators. The antisymmetric component of the resulting (closed-loop) control surface motion, $\delta_{TEO_{asy}}$, is shown in the figure. The antisymmetric wingtip accelerometer response, $\ddot{z}_{TIP_{asy}}$, was damped out in approximately 2 cycles after the command ended at 0.2 second. Small effects due to actuator asymmetries were apparent in the symmetric wingtip accelerometer response, $\ddot{z}_{TIP_{sym}}$. The small persistent oscillations in all responses were the result of a limit cycle arising from quantization effects.

Controller Implementation

Digital Implementation of Continuous Design

The control laws (all designed in the continuous domain), were implemented digitally, both in the simulation and in the digital controller, using a Tustin transformation with a 200 Hz sample rate. Prewarping was applied for those dynamic elements which required an analog/digital frequency response match at a frequency above 30 Hz. The prewarping was nonstandard. An iterative procedure was employed wherein a "desired" analog transfer function was specified, and a "modified" analog transfer function of the same form and order was sought which had a digital transform with frequency response close to that desired at and below a chosen frequency for a match.

Frequency Shift in Test Controller

A frequency shift was made in key controller dynamic elements for implementation during the test. The shift was based upon data gathered during the 1989 test which showed that the 1989 analytical model of the plant overpredicted the frequencies for the coalescing modes at flutter, for both symmetries, by nearly 2 Hz. It had also been shown that the predicted phase at the predicted frequency of peak response was in close agreement with the observed phase at the observed frequency of peak response.[4] The amplitude of accelerometer response to control deflections was also somewhat overpredicted. Table 1 indicates that, for the symmetric SISO controller, the situation where the actual frequencies and gain were lower than predicted was the least well tolerated combination of errors. For these reasons, the notch element (N_F) and the amplifier element (A_F) of the controller were shifted downward by 2 Hz for both symmetries prior to implementation for test.

Testing and Controller Updates

Impact of Early Testing on FSS

Early in the entry, investigators encountered an unexpected 64 Hz buzz of the trailing edge outboard control surfaces when the FSS loops were closed. New servovalves were installed for each actuator and an analog 64 Hz notch was inserted in each trailing edge outboard command channel. The buzz was removed, but approximately 13 degrees of phase lag at 10 Hz resulted.

Plant estimates were obtained below flutter during subcritical open-loop tests, and above flutter by analysis of results from post critical closed-loop tests of other FSS designs that had been tested earlier in the entry. The frequency-shifted controller designed prior to test was predicted, based upon the plant estimates, to be stabilizing. However, phase adjustments were made prior to closed-loop tests to improve robustness characteristics. The phase adjustments were made by modifying the highpass break frequencies and incorporating a lowpass filter, LP(c) (see figure 8, eq. (3) and table 2). The resulting symmetric law was then successfully tested to the tunnel limit in the free-to-roll configuration, reaching a dynamic pressure 25 percent above the observed (≈235 psf), open-loop flutter dynamic pressure.

Overnight Controller Reoptimization

An overnight reoptimization of the symmetric controller was accomplished during the wind-tunnel test using a hybrid of experimentally derived frequency responses for frequencies between 5 and 20 Hertz, and analytically predicted frequency responses for frequencies between 20 and 64 Hertz, all for a 285 psf condition. The frequency content for the excitation signal for the control surfaces used for feedback was limited to 20 Hertz and below, so that experimentally derived frequency responses above 20 Hertz were not available. An additional 40 Hz notch (N_2) was implemented digitally (after prewarping) on the output of HP_2 pertaining to the accelerometers other than the tip accelerometers (see figure 8 and table 2) to further safeguard against potential aggravation of the stability and response of higher frequency modes (the reoptimized controller utilized these inboard accelerometers more than the symmetric design based upon the analytic model did).

The SISO portion of the reoptimization did not include the variational terms (m=2-to-9 in eq. (4)). Two additional design variables were also included by allowing distinct numerator and denominator natural frequencies in the notch (N_F) and amplifier (A_F) dynamic elements. As mentioned previously, a 2 Hz frequency shift had been made in the controller dynamics in the flutter frequency region based upon data from a previous test. The reoptimization made only small additional shifts in the controller frequencies that had been selected prior to test. The parameters for the reoptimized controller, including

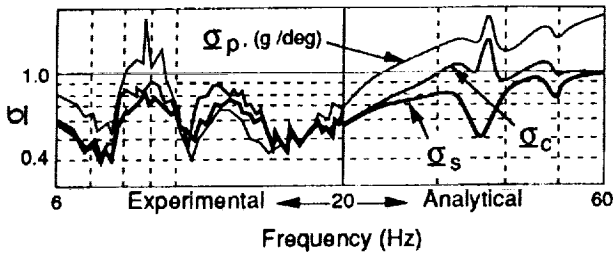

Fig. 10 Minimum singular values for reoptimized control law. (symmetric, 285 psf)

definition of all notches to be implemented digitally (after prewarping) are presented in table 2.

The reoptimization of this symmetric control law was accomplished overnight. In-flight excitation of the control surfaces and use of a computer that was two orders of magnitude faster would have allowed the plant frequency response estimates and controller redefinition to be completed quickly enough to perform a tuning type adaptation of the controller to changes in plant characteristics arising from slow (relative to the adaptation process) Mach number and dynamic pressure variations.

Figure 10 shows the predicted reoptimized controller performance based upon the hybrid experimental and analytical data. The local minima seen in the various minimum singular value curves are relatively well balanced in the 0-to-20 Hz frequency range with the smallest values of approximately 0.4 representing a significant level of robustness.

Test Results with Reoptimized Controller

The reoptimized controller was successfully tested with the AFW wind-tunnel model in both its free-to-roll and fixed-in-roll configurations. Results will now be shown that provide a more detailed description of the performance of the reoptimized controller.

With the reoptimized controller employed, symmetric flutter was again suppressed to the tunnel limit in the free-to-roll configuration. A maneuver load control (MLC) roll rate tracking system[18] was also active but was commanding zero roll rate. Figures 11 and 12 show absolute stability and stability robustness assessment information obtained in near-real-time during the test through the use of a Controller Performance Evaluation (CPE) analysis procedure.[5,19] These results were obtained using MIMO extensions to Fast Fourier Transform based SISO controller performance evaluation techniques.[20, 21]

Figure 11 shows MIMO Nyquist plots which, when accompanied by knowledge of open-loop stability characteristics, provide a definitive assessment of closed-loop

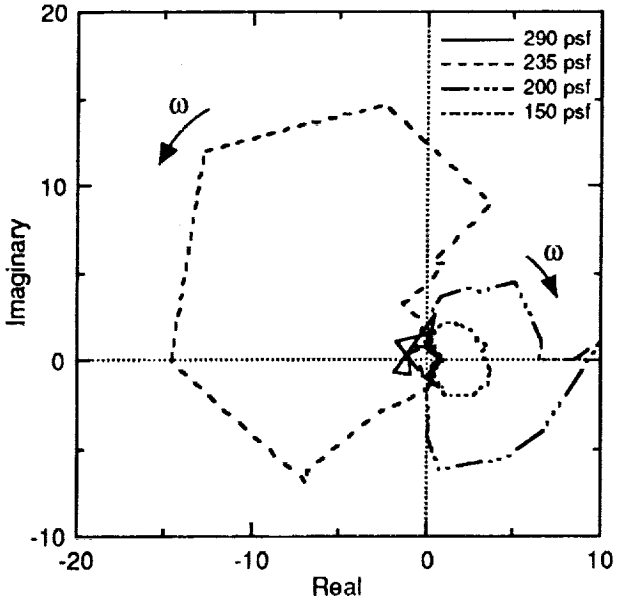

Fig. 11 Experimental MIMO Nyquist plots. (symmetric, reoptimized FSS with MLC)

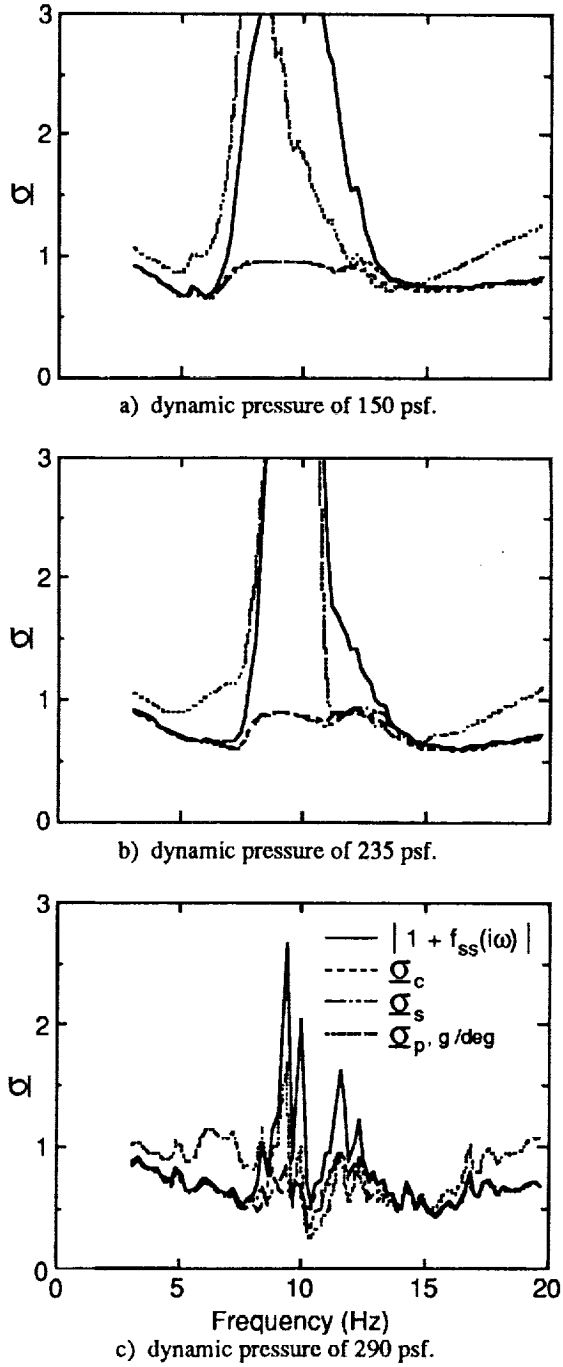

Fig. 12 Experimental singular values. (symmetric, reoptimized FSS with MLC)

stability. The MIMO Nyquist plots are polar plots of

$$\det[\, I_{2\times2} + K(i\omega)\, P(i\omega)\,] = \det[\, I_{4\times4} + P(i\omega)\, K(i\omega)\,]$$

or, equivalently, for a rank one loop transfer matrix,

$$= 1 + f_{ss}(i\omega).$$

The open-loop system was stable at the two lower dynamic pressures and unstable at the two higher dynamic pressures. Thus, figure 11 shows closed-loop stability at each condition (the origin is the critical point). The MIMO Nyquist curves are potentially nonconservative measures of stability robustness not just for the controller structure shown in figure 8, but in general. For rank one loop transfer matrices only, as was the case here (see K(s) in figure 8), the Nyquist curves directly display tolerances to uniform gain and phase errors on all channels or, equivalently, tolerances to gain and phase errors at the single strand point. Figure 12 provides additional stability robustness information.

In figure 12 minimum singular value curves $\underline{\sigma}_c(\omega)$ and $\underline{\sigma}_s(\omega)$ are shown for the return difference matrices at the plant input and output, respectively. These unstructured singular values correspond to the worst combination of independent multiplicative errors in the respective input or output channels. The magnitude of the MIMO Nyquist curve from figure 11 (plotted as the solid curve in figure 12) corresponds, for this rank one controller, to tolerance to uniform (dependent) errors and is an upper bound upon $\underline{\sigma}_c(\omega)$ and $\underline{\sigma}_s(\omega)$. Finally, a minimum singular value curve, $\underline{\sigma}_p(\omega)$, reflecting sensitivity to plant additive error, is shown. The singular value assessments of stability robustness are potentially quite conservative, since the likelihood of encountering the worst combination is not addressed. The potentially conservative nature of the singular value robustness assessments becomes more pronounced as the number of sensor or control channels is increased. Nevertheless, the singular values obtained for the MIMO controller compared well with those for SISO controllers that were tested during this entry,[12,22,23] particularly below 250 psf.

All curves for all dynamic pressures show a good balance in tolerance to phase lead errors ($5.5 < \omega < 7.5$ Hz) and phase lag errors ($14 < \omega < 16.5$ Hz). The curves for 290 psf exhibit noisy behavior because of a poor signal-to-noise ratio. Only small amplitude (±0.3 degree) input excitations could be made at 290 psf without exceeding torsional safety load limits. Nevertheless, it is apparent that the singular value minimum

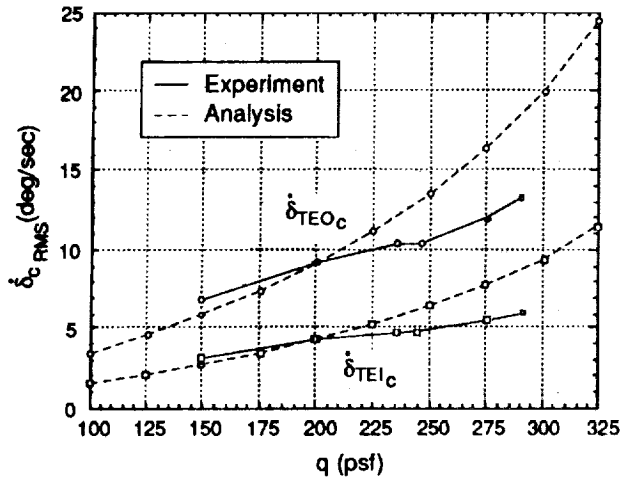

Fig. 13 RMS control rates due to turbulence.
(Symmetric, reoptimized FSS with MLC)

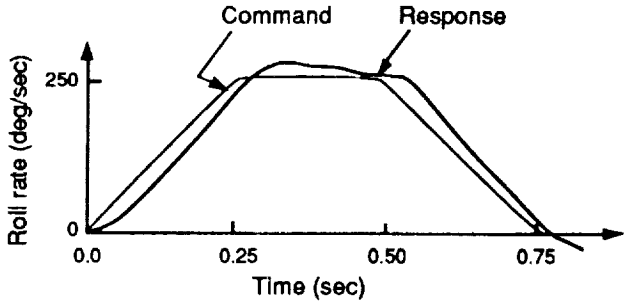

Fig. 14 Aggressive roll maneuver.
(11% beyond flutter dynamic pressure)

levels are significantly lower than those at the lower dynamic pressures. For 290 psf, the lowest singular values are at a frequency in close correspondence with the flutter frequency. This indicates that somewhat better performance could be expected with a higher gain controller.

Control surface RMS rates during a test run for the free-to-roll configuration are shown in figure 13 where they are contrasted with analytical predictions. Both actual and predicted RMS rates were well within the 50 deg/sec RMS design limit. There was qualitative agreement between analysis and experiment indicating that the analytically assumed gust environment was adequate for assessment of potential rate saturation problems.

Increasingly aggressive maneuvers (in terms of roll acceleration commands and dynamic pressures) were tested using a multifunction controller (i.e., both active flutter suppression and maneuver load control[18] were simultaneously employed). Figure 14 depicts the successful completion of the most aggressive maneuver. The maneuver commanded roll accelerations of 1000 deg/sec^2 until a roll rate of 250 deg/sec was achieved, held that rate until a 90 degree roll was completed (0-to-90 degrees in 0.5 sec), and then decelerated at approximately 1000 deg/sec^2. The maneuver was performed at a dynamic pressure 11 percent above the open-loop flutter boundary. The aggressive rolling maneuver did not appreciably affect the FSS peak control deflection or rate requirements.

A flutter suppression test was conducted with the AFW wind-tunnel model in the fixed-in-roll configuration. For this configuration, there was considerable disparity between the observed open-loop antisymmetric flutter dynamic pressure (219 psf) and that predicted with the design model chosen (252 psf for the pre-1989 model). Nevertheless, flutter was simultaneously suppressed in both symmetric and antisymmetric degrees-of-freedom to a dynamic pressure of 275 psf. This test was terminated at 275 psf because the turbulence induced loads were closely approaching preset safety limits on torsional loads. The remaining test time was too limited to allow generation of data for a full CPE analysis. However, stability and RMS control rate usage were determined at a number of test points. The RMS control rate requirements were well within the design limit being comparable to those of figure 13.

Conclusions

A multi-input/multi-output flutter suppression system for the Active Flexible Wing wind-tunnel model was developed in the continuous domain, implemented digitally and tested in the Langley Transonic Dynamics Tunnel. Optimization techniques were employed to define a controller that exhibited significant robustness to flutter frequency prediction errors and

to unstructured plant additive errors and unstructured multiplicative errors at the plant input and plant output.

The frequency domain based design approach readily permitted utilization of a combination of analytically predicted and experimentally estimated plant transfer matrices. An overnight reoptimization using combined experimental and analytical data was accomplished during the test. Stability robustness improvements resulted as compared with a stabilizing design based solely upon analytical predictions. The rapid redesign shows the potential, with a much faster computer than that used for controller implementation, for use of the approach in tuning type adaptive applications.

The reoptimized control law was tested. Symmetric flutter was suppressed to the tunnel limit. With a fixed-in-roll configuration, both symmetric and antisymmetric flutter were simultaneously suppressed to a dynamic pressure 26 percent above the antisymmetric open-loop boundary and 17 percent above the symmetric boundary. Turbulence induced loads which were approaching a preset torsional loads safety limit prevented attainment of the tunnel limit in this case. Simultaneous flutter suppression and maneuver load control were demonstrated during aggressive rolling maneuvers performed at a dynamic pressure 11 percent above the open-loop flutter boundary.

References

[1] Miller, G. D., "Active Flexible Wing (AFW) Technology," AFWAL-TR-1987.

[2] Perry, B., III, Cole, S. R., and Miller, G. D., "A Summary of the Active Flexible Wing Program," AIAA Paper 92-2080, *Proceedings of the Dynamics Specialists Conference*, AIAA, Dallas, TX, Apr. 1992.

[3] Hoadley, S. T., and McGraw, S. M., "The Multiple-Function Multi-Input/Multi-Output Digital Controller System for the AFW Wind-Tunnel Model," AIAA Paper 92-2083, *Proceedings of the Dynamics Specialists Conference*, AIAA, Dallas, TX, Apr. 1992.

[4] Adams, W. M., Christhilf, D. M., Waszak, M. R., Mukhopadhyay, V., and Srinathkumar, S., "Design, Test, and Evaluation of Three Active Flutter Suppression Controllers," NASA TM-4338, 1992.

[5] Pototzky, A. S., Wieseman, C. D., Hoadley, S. T., and Mukhopadhyay, V., "Development and Testing of Methodology for Evaluating the Performance of Multi-input/Multi-Output Digital Control Systems," NASA TM-102704, Aug. 1990.

[6] Peele, E. L., and Adams, W. M., Jr., "A Digital Program for Calculating the Interaction Between Flexible Structures, Unsteady Aerodynamics, and Active Controls," NASA TM-80040, Jan. 1979.

[7] Adams, W. M., Jr., Tiffany, S. H., Newsom, J. R., and Peele, E. L., "STABCAR: - A Program for Finding Characteristic Roots of Systems Having Transcendental Stability Matrices," NASA TP-2165, Jun. 1984.

[8] Tiffany, S. H., and Adams, W. M., Jr., "Nonlinear Programming Extensions to Rational Function Approximation Methods for Unsteady Aerodynamic Forces Which Allow Variable Selection of Constraints," NASA TP-2776, May 1988.

[9] Buttrill, C. S., Houck, J. A., and Heeg, J., "Hot Bench Simulation of the Active Flexible Wing Wind-Tunnel Model," AIAA Paper 90-3121, *Proceedings of Flight Simulation Technologies Conference*, AIAA, Dayton, OH, Sep. 1990.

[10] Buttrill, C. S., and Bacon, B. J., "Model Order Reduction Applied to a Hot-Bench Simulation of an Aeroelastic Wind-Tunnel Model," AIAA Paper 91-2935, *Proceedings of Flight Simulation Technologies Conference*, AIAA, New Orleans, LA, Aug. 1991.

[11] Buttrill, C. S., Bacon, B. J., Heeg, J., Houck, J. A., and Wood, D., "Simulation and Model Reduction for the AFW Program," AIAA Paper 92-2081, *Proceedings of the Dynamics Specialists Conference*, AIAA, Dallas, TX, Apr. 1992.

[12] Waszak, M. R., and Srinathkumar, S., "Flutter Suppression for the Active Flexible Wing: Control System Design and Experimental Validation," AIAA Paper 92-2097, *Proceedings of the Dynamics Specialists Conference*, AIAA, Dallas, TX, Apr. 1992.

[13] Davidon, W. C., "Variable Metric Method for Minimization," Argonne National Laboratory, Report ANL-5990, Rev., Nov. 1959.

[14] Fletcher, R., and Powell, M. J. D., "A Rapidly Convergent Method for Minimization," *Computer Journal*, Vol. 6, No. 2, Jul. 1963, pp. 163-168.

[15] Press, W. H., Flannery, B. P., Teukolsky, S. A., Vetterling, W. T., "Minimization or Maximization of Functions," *Numerical Recipes: The Art of Scientific Computing*, Cambridge University Press, Cambridge, MA, 1989, pp. 274-312.

[16] Park, S. K., "A Transformation Method for Constrained-Function Minimization," NASA TN D-7983, Nov. 1975.

[17] Doyle, J. C., and Stein, G., "Multivariable Feedback Design: Concepts for a Classical/Modern Synthesis," IEEE *Transactions on Automatic Control*, Vol. 26, February 1981, pp. 4-16.

[18] Moore, D. B., "Maneuver Load Control Using Optimized Feedforward Commands," AIAA Paper 92-2100, *Proceedings of the Dynamics Specialists Conference*, AIAA, Dallas, TX, Apr. 1992.

[19] Wieseman, C. D., Hoadley, S. T., and McGraw, S. M., "On-Line Analysis Capabilities Developed to Support the AFW Wind-Tunnel Tests," AIAA Paper 92-2084, *Proceedings of the Dynamics Specialists Conference*, AIAA, Dallas, TX, Apr. 1992.

[20] Edwards, J. W., "Flight Test Results of an Active Flutter Suppression System," *Journal of Aircraft*, Vol. 20, No. 3, March 1983, pp. 267-274.

[21] Adams, W. M., Jr., Tiffany, S. H., and Bardusch, R. E., "Active Suppression of an 'Apparent Shock Induced Instability'," AIAA Paper 87-0881, *Proceedings of 28th Structures, Structural Dynamics, and Materials Conference*, AIAA, Monterey, CA, Apr. 1987.

[22] Mukhopadhyay, V., "Flutter Suppression Digital Control Law Design and Testing for the AFW Wind-Tunnel Model," AIAA Paper 92-2095, *Proceedings of the Dynamics Specialists Conference*, AIAA, Dallas, TX, Apr. 1992.

[23] Klepl, M. J., "A Flutter Suppression System Using Strain Gauges Applied to Active Flexible Wing Technology: Design and Test," AIAA Paper 92-2098, *Proceedings of the Dynamics Specialists Conference*, AIAA, Dallas, TX, Apr. 1992.

REPORT DOCUMENTATION PAGE

Form Approved
OMB No. 0704-0188

1. AGENCY USE ONLY *(Leave blank)*	2. REPORT DATE	3. REPORT TYPE AND DATES COVERED
	May 1992	Technical Memorandum

4. TITLE AND SUBTITLE

Multifunction Tests of a Frequency Domain Based Flutter Suppression System

5. FUNDING NUMBERS

505-64-20-01

6. AUTHOR(S)

David M. Christhilf and William M. Adams, Jr.

7. PERFORMING ORGANIZATION NAME(S) AND ADDRESS(ES)

NASA Langley Research Center
Hampton, VA 23665-5225

8. PERFORMING ORGANIZATION REPORT NUMBER

9. SPONSORING / MONITORING AGENCY NAME(S) AND ADDRESS(ES)

National Aeronautics and Space Administration
Washington, DC 20546-0001

10. SPONSORING / MONITORING AGENCY REPORT NUMBER

NASA TM-107615

11. SUPPLEMENTARY NOTES

Christhilf: Lockheed Engineering & Sciences Co., Hampton, VA; and Adams: Langley Research Center, Hampton, VA. Presented as AIAA Paper No. 92-2096 at the Dynamics Specialists Conference; Dallas, TX; April 16-17, 1992.

12a. DISTRIBUTION / AVAILABILITY STATEMENT

Unclassified-Unlimited

Subject Categories 08, 05

12b. DISTRIBUTION CODE

13. ABSTRACT ***(Maximum 200 words)***

This paper describes the process of analysis, design, digital implementation and subsonic testing of an active controls flutter suppression system for a full span, free-to-roll wind-tunnel model of an advanced fighter concept. The design technique employed a frequency domain representation of the plant and used optimization techniques to generate a robust multi-input/multi-output controller. During testing in a fixed-in-roll configuration, simultaneous suppression of both symmetric and antisymmetric flutter was successfully demonstrated. For a free-to-roll configuration, symmetric flutter was suppressed to the limit of the tunnel test envelope. During aggressive rolling maneuvers above the open-loop flutter boundary, simultaneous flutter suppression and maneuver load control were demonstrated. Finally, the flutter suppression controller was reoptimized overnight during the test using combined experimental and analytical frequency domain data, resulting in improved stability robustness.

14. SUBJECT TERMS

active flutter suppression, frequency domain, multi-input/multi-output, constrained optimization design, robustness, digital implementation, Active Flexible Wing, wind-tunnel test, multifunction controller testing

15. NUMBER OF PAGES

11

16. PRICE CODE

A03

17. SECURITY CLASSIFICATION OF REPORT	18. SECURITY CLASSIFICATION OF THIS PAGE	19. SECURITY CLASSIFICATION OF ABSTRACT	20. LIMITATION OF ABSTRACT
Unclassified	Unclassified		